REPORT DOCUMENTATION PAGE

Form Approved
OMB No. 0704-0188

1. REPORT DATE *(DD-MM-YYYY)*
05-09-2005

2. REPORT TYPE
REPRINT

3. DATES COVERED *(From - To)*

4. TITLE AND SUBTITLE
Non-equilibrium Radiative Transfer in Structured Atmospheres

5a. CONTRACT NUMBER

5b. GRANT NUMBER

5c. PROGRAM ELEMENT NUMBER
62601F

6. AUTHOR(S)
R.H. Picard[1], J.R. Winick.[1], and P.P. Wintersteiner[2]

5d. PROJECT NUMBER
2301

5e. TASK NUMBER
BD

5f. WORK UNIT NUMBER
A1

7. PERFORMING ORGANIZATION NAME(S) AND ADDRESS(ES)

Air Force Research Laboratory
29 Randolph Road
Hanscom AFB, MA 01731-3010

8. PERFORMING ORGANIZATION REPORT NUMBER

AFRL-VS-HA-TR-2005-1115

9. SPONSORING / MONITORING AGENCY NAME(S) AND ADDRESS(ES)

10. SPONSOR/MONITOR'S ACRONYM(S)

AFRL/VSBYB

11. SPONSOR/MONITOR'S REPORT NUMBER(S)

12. DISTRIBUTION / AVAILABILITY STATEMENT
Approved for Public Release; Distribution Unlimited.

[1] Air Force Research Laboratory, Hanscom AFB, MA [2] ARCON Corporation, Waltham, MA

13. SUPPLEMENTARY NOTES
Reprinted from: Proceedings of SPIE Vol. 4539 (2002), Pages 454 - 468

14. ABSTRACT

The nonequilibrium middle and upper atmosphere are very dynamic regions that are structured vertically and horizontally by the presence of persistent temperature inversion layers and by the passage of both atmospheric gravity waves and transient frontal disturbances or bores. The infrared emissions from this part of the atmosphere are already typically not in local thermodynamic equilibrium (LTE) and are further perturbed by the presence of this pervasive atmospheric structure. The inevitable result is highly structured atmospheric emissions that reflect the structure of the atmosphere. Understanding the structure of the atmosphere is essential to understanding the structure of the radiation that it emits. At the same time understanding how atmospheric structure perturbs atmospheric radiation provides a means to sense the perturbing atmospheric processes remotely. We examine methods to calculate the LTE / non-LTE radiative response to temporal and spatial variations of the atmosphere and give examples of applications. We also compare our results with existing field data. Finally, we discuss a proposed new NASA optical / infrared experiment (Waves Explorer) to sense atmospheric gravity waves remotely from earth orbit on a global basis and characterize their sources.

15. SUBJECT TERMS

Radiative transfer Atmospheric structure

16. SECURITY CLASSIFICATION OF:

a. REPORT	**b. ABSTRACT**	**c. THIS PAGE**	**17. LIMITATION OF ABSTRACT**	**18. NUMBER OF PAGES**	**19a. NAME OF RESPONSIBLE PERSON**
UNCLAS	UNCLAS	UNCLAS	SAR	15	Richard H. Picard
					19b. TELEPHONE NUMBER *(include area code)* 781-377-2222

Standard Form 298 (Rev. 8-98)
Prescribed by ANSI Std. 239.18

AFRL-VS-HA-TR-2005-1115

Non-equilibrium radiative transfer in structured atmospheres

R. H. Picard*[a], J. R. Winick*[a], P. P. Wintersteiner**[b]
[a]Air Force Research Laboratory; [b]ARCON Corp.

ABSTRACT

The nonequilibrium middle and upper atmosphere are very dynamic regions that are structured vertically and horizontally by the presence of persistent temperature inversion layers and by the passage of both atmospheric gravity waves and transient frontal disturbances or bores. The infrared emissions from this part of the atmosphere are already typically not in local thermodynamic equilibrium (LTE) and are further perturbed by the presence of this pervasive atmospheric structure. The inevitable result is highly structured atmospheric emissions that reflect the structure of the atmosphere. Understanding the structure of the atmosphere is essential to understanding the structure of the radiation that it emits. At the same time understanding how atmospheric structure perturbs atmospheric radiation provides a means to sense the perturbing atmospheric processes remotely. We examine methods to calculate the LTE / non-LTE radiative response to temporal and spatial variations of the atmosphere and give examples of applications. We also compare our results with existing field data. Finally, we discuss a proposed new NASA optical / infrared experiment (Waves Explorer) to sense atmospheric gravity waves remotely from earth orbit on a global basis and characterize their sources.

Keywords: Radiative transfer, atmospheric structure

1. INTRODUCTION

Infrared atmospheric radiance seen from space is influenced by the structure of the atmosphere on many spatial scales. Satellite infrared images of cloud structure are familiar to anyone who watches televised meteorological forecasts. In a similar way, infrared emissions are sensitive to wave perturbations in the clear atmosphere. Atmospheric gravity waves (GWs) are nearly always seen in the atmosphere and result in atmospheric radiance structure. Since they tend to grow in amplitude with height, they are especially important in the upper stratosphere and in mesosphere / lower-thermosphere (MLT) region. While GWs tend to be extended atmospheric perturbations in both the vertical and horizontal dimensions, atmospheric radiance seen from space is also perturbed, in some cases quite severely, by other types of atmospheric perturbations that are more localized.

Knowledge of radiance structure resulting from atmospheric perturbations is important to remote sensing in two different ways. First, this radiance structure is a background against which space observations of the earth or of airborne/spaceborne objects along any line-of-sight (LOS) intersecting the atmosphere must be made. The result can be a false positive signal of the desired target object or surface property (false alarm) or a missed detection of the object or property. On the other hand, knowledge of the radiative response of an atmospheric perturbation can provide a powerful means to sense the perturbing process remotely, and this is the aspect we wish to emphasize in this paper. By understanding the properties of the atmospheric perturbations and of the radiative transfer (RT) process in a structured atmosphere, we hope to shed some light on the ability to do such remote sensing.

We will review the sources of atmospheric structure, both spatially extended and localized, in Section 2. Section 3 will discuss the observation of IR emissions from space. Section 4 will continue with a discussion of structured IR emissions as seen from space. Wave observations from space will be reviewed, including a series of recent IR observations by the MSX (Midcourse Space Experiment) satellite. We complete the section with a discussion of the RT of localized perturbations, in particular layer structures localized in the vertical. Section 5 will briefly describe a concept for a proposed GW survey satellite employing IR remote sensing of waves, and Section 6 will present conclusions.

---

*mailto:richard.picard@hanscom.af.mil; phone 1-781-377-2222; fax 1-781-377-8900; Air Force Research Laboratory, Space Vehicles Dir., 29 Randolph Road, Hanscom AFB, MA 01731-3010, USA; **ARCON Corp., 260 Bear Hill Road, Waltham, MA 02454, USA

Remote Sensing of Clouds and the Atmosphere VI, Klaus Schäfer, Olga Lado-Bordowsky, Adolfo Comeron, Michel R. Carleer, Janet S. Fender, Editors, Proceedings of SPIE Vol. 4539 (2002) © 2002 SPIE · 0277-786X/02/$15.00

2. SOURCES OF ATMOSPHERIC STRUCTURE

A large number of atmospheric processes affect the radiative emission of the atmosphere and its space-time structure. Among the most important of these are atmospheric disturbances associated with atmospheric GWs. These wave perturbations may be either quasi-periodic disturbances due to isolated waves (for example[1, 2]) or broadband perturbations resulting in continuous spectra and associated with saturated GWs.[3, 4] The largest radiative responses, however, are often associated with a number of different spatially localized atmospheric perturbations that result in either rapid vertical or horizontal changes in atmospheric properties affecting the emission or transmission of radiation. These include fronts or bores and temperature inversion layers, as well as solar terminator, thundercloud-induced perturbations, polar mesospheric clouds, discrete auroral arcs, and minor-species laminae. We discuss the first two of these below in Section 2.2 in more detail.

2.1 Atmospheric gravity waves

Atmospheric GWs (see, for example[5]) have temporal and spatial scales between those of turbulence at smaller scales and planetary waves and tides at larger scales. They play important roles in the momentum and energy budgets of the mesosphere and lower thermosphere (MLT), accelerating mean flows and strongly affecting the nature of the global circulation. They amplify and modulate planetary waves and tides, producing combination tones and sidebands. And they break, giving rise to turbulence and thus affecting diffusion and other transport processes. In general, waves are launched by tropospheric sources, propagate upward growing in amplitude, then saturate, breaking and converting energy to other modes by wave-wave interactions before finally dissipating. Tropospheric wave sources include orographic uplifting (mountain waves), convective activity (thunderstorms), jet streams, fronts, and geostrophic adjustment. The smallest scales saturate at the lowest altitudes, with progressively larger scale waves saturating at higher altitudes. The saturated waves deposit energy and momentum affecting the atmospheric mean state and lead to local variability. Generally, the most profound effects of the saturating waves are felt in the MLT region. While wave temperature-perturbation amplitudes are typically ~1-2 K in the stratosphere, they can be 5-10 K or more at the mesopause.

Atmospheric waves have turned out to be a prime mechanism leading to optical / IR radiance structure. They do so by perturbing the atmospheric temperature and density, which in turn results in perturbations in the number density of radiating states and in radiance perturbations. This is true both for airglow emissions[6, 7] and for LTE and non-LTE thermal emissions.

2.2 Spatially localized atmospheric perturbations

Perturbations affecting both the vertical and horizontal structure of the atmosphere are quite common. Both of these types of perturbations were observed in a recent campaign dedicated to MLT structure. This is the ALOHA 93 (Airborne Lidar Observations of Hawaiian Airglow 1993) Campaign, based at the Air Force Maui Optical Station atop Haleakala, Hawaii. The observations included the following:

(1) Prominent temperature inversion (TI) layers with tidal progressions were found by means of Rayleigh and Na resonance lidars.[8, 9] Other investigators have found evidence that inversion layers are very common, persistent features of the MLT temperature field, even surviving in seasonally averaged data under the right conditions. The TI layers observed by *Dao et al.*[8] and *Tao and Gardner*[9] on one of the Campaign nights have been explained[10] as resulting from GW critical-level interactions. A critical-level occurs when the wave's phase speed is equal to the background wind. At a critical level the wave can interact with the mean flow, accelerating it. This results in large shears which can be unstable, giving rise to turbulence and eventually to atmospheric heating.

(2) A spectacular front or wall of structure traveling at 75 m/s across the sky from NW to SE was observed by a four-color CCD airglow imager on the ground at Haleakala.[11] In the lower altitude emissions (OH Meinel bands and Na D lines) the field was dark and unstructured ahead of the front and bright behind the front with prominent periodic wave structure. For the higher altitude emissions (atomic-oxygen green line and O_2 Atmospheric bands), the field was complementary, that is bright ahead of the front, dark and wave-structured behind it. *Dewan and Picard*[12] showed by a simple analytic model that this occurrence could be explained as an example of a bore phenomenon, familiar to us from the tidally dependent bores occurring in river channels. The bore is actually a phase front associated with a transient wave disturbance of the MLT region and occurring in a wave duct formed by the structure of the temperature and wind fields. The ducting has been attributed by *Dewan and Picard*[12] to a temperature-inversion layer similar to one mentioned above, although wind-shear layers can also play an important role. In a recent paper *Dewan and Picard*[13]

have shown that the GW critical layer phenomenon can be the source of not only the ducting structure but also the body force required to launch the bore.

Both of these effects are expected to give rise to large gradients in the volume emission rate—vertical gradients in case (1) and horizontal gradients in case (2)—and, therefore, gradients in the observed radiance. We consider the radiative structure arising in case (1), as well as the radiative structure resulting from atmospheric GWs, in the following sections.

3. INFRARED ATMOSPHERIC EMISSION SEEN FROM SPACE

Infrared atmospheric emissions in the mid-wave region of the infrared (MWIR, 3-6 μm, 3300-1650 cm^{-1}) are largely composed of rovibrational bands from the ground electronic state of molecules. Among the strongest bands emitting in this region are the ν_3 bands of CO_2, whose fundamental transition is near 4.26 μm (2349 cm^{-1}) and which are characterized by radiating states with one quantum of asymmetric stretch. The bands also include isotopic and hot bands, and in the nonequilibrium daytime atmosphere, solar fluorescent bands.

The strong ν_3 bands have lines which are optically thick everywhere below 100 km altitude, and radiative transfer calculations consisting of solutions of the equation of transfer are required to predict spectral radiances.[14] In the lower atmosphere, collisions are usually frequent enough to keep the radiating levels in LTE (local thermodynamic equilibrium), and the populations of the radiating rovibrational states are given by the Planck source function. This is certainly true for most bands below the stratopause (about 50 km altitude). At higher altitude, collisions are too infrequent to dominate the production and loss processes for the radiating states. Then the radiating levels are non-LTE, and separate calculations of the nonequilibrium radiating state populations are required through rate equations that take into account all production and loss processes. Generally, for a sub-limb, or below-the-horizon (BTH), line-of-sight (LOS) non-LTE effects are relatively minor, while for a limb, or above-the-horizon (ATH), LOS with a tangent altitude above 60 km non-LTE effects must be included. Non-LTE IR radiative-transfer models have been formulated by us[15, 16] and others for a number of radiators including CO_2 ν_3 (4.3 μm) and ν_2 (15 μm) bands.

The contributions of different volume elements along the LOS to the radiance seen by the sensor are captured in the contribution function (CF). The CF is inherently a function of distance of the volume element along the LOS from the sensor but can be viewed, alternatively, as a function of altitude of the emitting volume element. For a BTH LOS from Earth orbit, the CF will not generally peak at the ground where the emitter density is maximum, but at some finite altitude determined by the interplay between the increase in emitter density and the increasing exponential attenuation of radiance with distance from the emitting element. Weaker isotopic and hot bands will be attenuated less than the main band and will be associated with CF peaks further from the sensor and at lower altitude. Similarly, for a limb or ATH LOS the CF will not generally peak at the tangent point, which has the largest geometrical weight, but at a point closer to the sensor along the LOS. Typical CFs for limb and sub-limb LOS are shown in *Picard et al.*[17] for cases appropriate to the 4.3-μm channels (B1 and B2) of the SPIRIT 3 radiometer on the MSX (Midcourse Space Experiment) satellite.

4. ATMOSPHERIC RADIATIVE STRUCTURE SEEN FROM SPACE

The mechanism whereby atmospheric structure leads to structure in the emitted and transmitted radiance is straightforward. The processes that structure the atmosphere typically produce perturbations in the atmospheric temperature and density and perhaps also in the volume mixing ratios of radiatively important minor species. These perturbations result in perturbations of the populations of radiating states and, in turn, in perturbations of the volume emission rate and of the resulting radiance. This overall description applies whether the emissions are LTE or non-LTE. Since radiative transport is generally a smoothing process, one would expect the radiance structure to be smoother than the structure of the underlying atmosphere. Radiative transport describes two types of processes resulting in the smoothing of atmospheric radiance structure: 1) integration of the volume emission rate along the line-of-sight (LOS), which smoothes out structure in the LOS direction, and 2) scattering processes resulting in changes in the direction of propagation and, hence, smoothing of the transverse structure. Process (2) can be quite important at short wavelength and in the lower atmosphere, but is not usually important in the IR at altitudes above 30 km. In the non-LTE region there is yet a third process of importance to consider which smoothes radiance fluctuations. This is the process of emission followed by nonlocal reabsorption, that is reabsorption at some other spatial location. The result of this process is that the perturbations of radiating level populations or vibrational temperatures are smaller than the temperature or density perturbations, ultimately resulting in further smoothing of the horizontal and vertical structure in the radiance perturbations.

When the emission is LTE, the process is particularly simple to describe, yet it is still challenging to carry out detailed computations. The simplest case occurs when one considers the atmosphere to be a greybody within the bandpass concerned and the wave-induced temperature perturbation is small. Then the spectral radiance R_ν at wavenumber ν obeys the Planck law, and the linear response to a temperature perturbation is proportional to the temperature sensitivity function,

$$\frac{dR_\nu}{dT} = \frac{h^2 c^3 \nu^4 \varepsilon}{2k_B T^2 \sinh^2\left(hc\nu / 2k_B T\right)} ,$$

The normalized sensitivity function is given by

$$\eta \equiv \frac{T_0}{R_{\nu 0}} \frac{dR_{\nu 0}}{dT_0} = \frac{R_\nu' / R_{\nu 0}}{T' / T_0} \approx \frac{hc\nu}{k_B T_0},$$

when $hc\nu \gg k_B T_0$. Here, the zero subscripts denote unperturbed fields and primes indicate linear perturbation amplitudes. In the upper stratosphere, $T_0 \approx 250$ K, so that for $\lambda = \nu^{-1} = 4.3$ µm, we have $\eta \approx 13$. Hence, the radiance fluctuations are amplified by an order of magnitude compared to the temperature fluctuations, indicating an extreme sensitivity to temperature fluctuations. There is also a much smaller sensitivity of the radiance field to density perturbations, which can often be ignored.

4.1 Wave observations from space

There is a long history of GW observations from the ground, using microbarographs, radar, and lidar. Optical airglow observations using spectrometers to determine Doppler or rotational temperature and low-light-level imagers observing airglow layers have also contributed greatly to our knowledge of MLT GW fields. Observations of GWs have also been made from space in the ultraviolet, visible-to-near-IR, long-wave IR, and millimeter-wave portions of the spectrum. Several of the observations report waves in airglow emission layers at 85-100 km. *Hersé*[18] reported waves in broadband visible / near-IR imaging of the earthlimb, which he attributed to OH Meinel-band emission but are now thought to be due to the O_2 Atmospheric bands. *Ross et al.*[19] observed waves in the UV region from Herzberg-I limb emission. *Mende et al.*[21, 22] observed GWs in O_2 Atmospheric-band (0, 0) emission at 762 nm from the Space Shuttle in a BTH high-nadir-angle observational mode. Finally, UARS/MLS researchers[22-24] observed fluctuations attributed to GW in low earthlimb observations in a number of channels of the temperature-sounding line (63 GHz O_2 emission) having CFs peaking from 28-80 km.

Turning to the IR spectrum, *Fetzer and Gille*[25] observed fluctuations attributed to long-horizontal-wavelength (>~200 km) inertio-gravity waves in LIMS limb soundings using the CO_2 15-µm temperature channel. Two of our publications[17, 2] report MSX satellite observations of 4.3-µm GW structure in BTH and ATH scans. The MSX observations differ in that they report, for the first time, high-resolution imagery of waves at 4.3 µm in the MWIR and at stratospheric altitudes near 40 km. By contrast, all previous measurements except those of *Fetzer and Gille*[25] and the MLS team have looked at MLT airglow layers in the UV to very near IR spectral range.

4.2 MSX gravity-wave observations

During the period from May 1996 to February 1997, the MSX satellite,[26, 27] carrying the SPIRIT 3 radiometer, accumulated a number of spatial radiance maps showing evidence of GW structure in the upper stratosphere (approximately 50 BTH and 10 ATH maps). The SPIRIT-3 radiometer, constructed by Utah State University's Space Dynamics Laboratory, has a focal plane array consisting of 192 elements in a column, covering a total angular extent of 1°. With the MSX near-circular orbit at 900-km altitude, individual array elements cover 80 m on the earth in nadir view, roughly 200 m at 57° nadir angle, and 300 m in the limb. The 4.3–µm B band includes narrowband (B1) and wideband (B2) channels, covering 4.22-4.36 µm and 4.24-4.45 µm, respectively. In one data-collection mode (EL09), the spacecraft looks perpendicular to the velocity vector at constant nadir angle for approximately 20 min, with the motion of the spacecraft (about 7 km/ s) providing a spatial scan of radiance. A large percentage of the data from both B1 and B2 channels shows evidence of distinct wavelike structure.

Figures 1 and 2 show typical MSX radiance maps showing BTH wave structure at 4.3 µm. *Picard et al.*[17] argue that such structure is due to GWs near 40 km altitude and show how the wave structure is distinguished from cloud structure. In Figure1,[2] recorded over India (23N) on 2 October 1996 at a nadir angle of 61° for the bottom pixel, a single spherical ring pattern from a point source dominates the structure. *Dewan et al.*[2] show that this wave was generated by an isolated thunderstorm located at the center of the ring pattern one hour earlier. When projected onto a reference sphere at an altitude of 40 km, the image covers an area 410 km (vertical) by 760 km (horizontal) in extent. By contrast, the structure in Figure 2, while still distinctly wavelike, appears to consist of multiple superposed monochromatic GW fields. The image was recorded on 27 August 1996 over the Indian subcontinent and Tibet at a nadir angle of 57° and covers an area of ~ 125 km by 375 km. Discrete wavelike structure also appears in the nadir and in the sparser earthlimb (ATH) data set. However, the BTH data at very high nadir angles, near the horizon (nadir angle of horizon = 61.4°) are especially rich in wave structure while minimizing the possibility of contamination by clouds.[17]

Other bands besides the 4.3-µm band are also susceptible to wave-structure perturbations. In Figure 3 we show successive limb profiles of the MSX 15- µm band at 30-s intervals covering tangent heights of 80-130 km and a total distance along track of 3000 km. Prominent wavelike perturbations are visible in the lower thermosphere between 90 and 110 km, where a ledge or secondary peak in the radiance profile is commonly seen. There is also some evidence present at later times below 80 km of a descending phase front, which would be associated with an upward-propagating large-scale GW. Changes of a factor of two in radiance are seen near 110 km over scales of a few hundred km in the horizontal. It is not surprising that smaller scales are suppressed, since they will tend to cancel out along the long limb LOS, unless the LOS should happen to be favorably aligned along phase fronts of the dominant wave disturbances, which form a Venetian-blind-like structure. The CO_2 15-µm band is non-LTE above about 90km, and, for a number of reasons, the non-LTE response must be smaller than the LTE response. Hence, the large radiance fluctuations seen represent significant wave-induced changes in atmospheric temperature structure.

Similar large variations are not observed simultaneously in the 4.3-µm channel in this altitude range. This difference can be explained by noting that in the ATH views of the non-LTE MLT region, the 4.3-µm daytime emission is not very sensitive to local temperature perturbations, since it is dominated by fluorescence following solar excitation. (This is in contrast to the 4.3-µm LTE upper-stratospheric emission that is prominent in the BTH data and is mostly sensitive to local temperature perturbations.) For tangent heights in the MLT range, the 4.3-µm radiance variations should be proportional to variations in the LOS column density of CO_2. Therefore, the absence of 4.3-µm structure rules out CO_2 density changes as the primary cause of the observed radiance perturbations at 15 µm. The 15-µm band, however, is quite sensitive to the temperature and the atomic oxygen density, not just the CO_2 density whose variation is constrained by the 4.3-µm channel.

4.3 Radiative transfer and gravity-wave structure

We calculate explicitly the B-band CFs, or layer radiances per unit altitude, for the MSX viewing geometry using FASE, a line-by-line radiative-transfer code derived from FASCODE.[28] The procedure is the following: (1) Calculate monochromatic spectral radiance (about 4×10^{-4} cm^{-1} resolution) over the B-band bandpass (2225-2475 cm^{-1}) from each layer boundary, spaced 1 km apart, to the effective top of the atmosphere (120 km). (2) Smooth the resulting 120 LOS radiances to a resolution of 0.4 cm^{-1}. (3) Obtain layer radiances and CFs by subtracting adjacent LOS radiances and dividing by layer thickness.

Figure 4 shows the non-LTE CFs calculated for the MSX B1 band, the narrower of the two 4.3-µm bands, and for three different model atmospheres, assuming a nadir angle of 57° and a solar zenith angle (SZA) of 60°. As already discussed, the CF peaks near 40 km in the LTE region, with a secondary non-LTE peak near 80 km.[17] The primary peak is a strong function of stratopause temperature, as seen by comparing the polar summer and polar winter profiles, while the non-LTE peak is nearly independent of temperature. The CFs do not extend down into the troposphere and, hence, should be insensitive to cloud-induced radiance perturbations.[17] Figure 5 compares the non-LTE and LTE CFs for the US Standard Atmosphere and reaffirms the non-LTE origin of the secondary peak. It is found that the non-LTE contribution occurs between 60 and 110 km and is independent of latitude and season, depending almost entirely on the SZA. *Picard et al.*[17]

deemed the non-LTE emission from the MLT to be an insignificant contributor to both the total radiance and the wave-induced radiance for normal atmospheric GW growth rates with height, based on simulation of a particular wave event with SZA=73°. However, the results of the current analysis show that the non-LTE contribution may have a significant contribution in daytime only for SZAs < 65°-70°, depending, for the case of the wave-induced radiance, on the extent to which wave saturation slows down the exponential wave growth.

FASCODE and FASE are intrinsically one-dimensional RT codes, not designed for horizontal-structure calculations, but useful nonetheless if the atmospheric state is completely characterized everywhere on the LOS. Hence, we propose to input a fictitious "model atmosphere" to FASE consisting of wave-perturbed atmospheric parameters specified at points along the LOS. The calculation is computationally intensive, but an approximation based on CFs, calculated for particular nadir angles, can produce nearly the same result almost instantaneously. The method involves precalculating and storing the CFs for the unperturbed atmosphere, then calculating the wave perturbation fields for temperature, pressure, density, and species mixing ratios in the Eulerian frame at every point along the LOS. Finally, the perturbed volume emission rate is calculated from the temperature and species-density perturbations, multiplied by the stored CF, and integrated over the LOS to obtain the perturbed radiance.

It is assumed that the GW period is short enough that the wave motion can be treated as adiabatic and that the pressure and density perturbations are related to the temperature perturbation by the isothermal GW polarization relations.[30] It is further assumed in the approximate calculation that (a) only the source function of the equation of transfer is perturbed and that there is no perturbation of the opacity by the wave, (b) the wave perturbation is linear, and (c) the wave response is only LTE. Assumption (a) is justified by noting that the perturbations of the opacity will tend to cancel, at least partially, in the LOS integration, and assumption (b) follows from the small amplitude of the wave perturbations near 40 km, typically $\lesssim$2% inferred from the MSX data. We find that the results obtained for the wave response by this simple approximate method compare well with the results of the full FASE calculation.

Since broadband filters, such as the B1 and B2 band MSX filters, encompass a large range of optical depths as one moves from the center to the far-wing region of the lines in the passband, the corresponding CFs end up being relatively broad with widths of 15-20 km. Many of the GW we are concerned with have vertical wavelengths that are considerably less than this, so that there will be a difference in radiance resulting from a given wave disturbance depending on whether the line-of-sight is aligned with a phase front or not. The maximum radiance will be seen when the LOS is wavefront-aligned, while a minimum response will involve destructive interference or cancellation of effects from opposite phase regions of the wave. This effect of varying wave response for the radiance depending on the observing direction has been called "observational filtering" by *Alexander*.[29] It follows that the depression angle β of the LOS to the local horizontal at the observation, or target, altitude z_t (usually chosen to be at the peak altitude of the CF, or around 40 km in MSX B band) is critical. In the MSX BTH viewing geometry an observer viewing GWs from an altitude z_o in a direction with nadir angle α will be associated with a local depression angle at the target altitude of

$$\beta = \cos^{-1}\left(\frac{R_E + z_m}{R_E + z_t}\sin\alpha\right),$$

where R_E is the local earth radius. As the nadir angle varies from 0° to the angle such that the LOS is tangent to the reference sphere at altitude z_t, β varies from 90° to 0°. For example, at $\alpha = 57°$, for the 900-km orbit altitude of MSX, $\beta = 18°$, which would allow one to selectively see radiance from waves having their vertical and horizontal wavelengths in the ratio $\lambda_z/\lambda_x = \tan 18° = 0.32$. From the approximate GW dispersion relation,[30] $\omega / N = \cos\theta$, where N is the Brunt-Vaisälä frequency and θ is the elevation angle of the wave vector, we conclude that observational filtering leads directly to a filtering in wave frequency or period.

The cancellation effect is shown in Figure 6. Here we look at the temperature perturbations for the plane wave with λ_x=10 km and $\lambda_z=\lambda_x/0.32$=32 km. The LOS at $\alpha = 57°$ is aligned with the phase fronts when the wave is propagating toward the observer and cuts across wavefronts when the wave vector is away from the observer. The effect at different altitudes is always in phase for the aligned case and oscillates rapidly with height for the misaligned case. The corresponding radiance response is shown in Figure 7 for the aligned and misaligned cases, and similar remarks can be made about the constructive and destructive interference of wave effects in these two cases.

4.4 Radiative transfer and localized layer structure

Sharply layered structures in temperature and minor-species density abound in all regions of the atmosphere and have important radiative implications. Here we consider the radiance perturbations due to both idealized and realistic TI layers, which are persistent features seen in atmospheric temperature data, yet are not reflected in standard model atmospheres. Band models generally find it difficult to deal with the thin shells required to model the non-LTE RT, so we use the line-by-line ARC (Atmospheric Radiance Code) model for CO_2 ν_3 and ν_2 radiative calculations at 4.3 and 15 μm.

Figure 8 shows the effect on the nighttime CO_2 ν_3 vibrational temperature (T_{vib}) of a T_{kin}=+40 K kinetic temperature perturbation 1-km wide at an altitude of 70 km. The figure shows the values of T_{vib} for a number of hot and isotopic bands in addition to the fundamental band. This layer results in an increase by a factor of two of the limb radiance for tangent heights near and above the layer altitude, as well as a huge perturbation in the vertical gradient of radiance. There is an even larger effect on the values of T_{vib} for ν_2 states. We see from Figure 8 that there is a large effect of the TI layer on T_{vib} not only near the layer perturbation but also *at all altitudes above the layer*. This is because radiative emission and reabsorption transports the excitation out of the region of the temperature perturbation and in particular to higher altitudes well above the temperature perturbation region.

We also find that realistic lidar temperature profiles showing TI layers, such as the profile from the ALOHA-93 Campaign shown in Figure 9,[8] have significant IR radiative impacts. TI layers are present in Figure 9 near 88 and 66 km. Also shown is a corresponding smooth profile generated from the MSIS model. These layers, with a maximum perturbation of ~40 K for the upper layer, have significant impact on both the radiance and the radiance gradient (Figure 10), once again extending up to high altitude well above the perturbation region.

5. WAVES EXPLORER: A PROPOSED GRAVITY-WAVE SURVEY SATELLITE

Waves Explorer (Figure 11) is a satellite experiment concept, conceived by a team headed by Gary Swenson at the University of Illinois and proposed to NASA, to observe and quantify the effects of small-scale waves in the earth's atmosphere.[31] During its two-year proposed life, it will monitor such waves from the source region in the troposphere and lower stratosphere to the MLT region where the waves have their most dramatic effects. Sensors will observe airglow emissions in BTH and limb modes to measure wave-perturbed emission structure in the MLT and also use IR bands to measure tropospheric high-altitude cloud tops as proxies for convective wave sources. In particular, it will monitor waves in the 40-km altitude range at 4.3 μm using a modification of the MSX observation technique. The Waves Explorer 4.3-μm BTH instrument, known as SWAPI and designed at Lockheed-Martin Advanced Technology Center, is one of five onboard instruments.[32] By using narrow bandpasses in various portions of the line having different opacities (line core, line wing, far wing, ...), SWAPI will be able to probe waves in the vicinity of a number of different altitudes centered between 25 and 45 km. SWAPI will make use of the observational filtering effect for broad CFs mentioned in Section 4.3 to distinguish small-scale waves with various periods. This will be accomplished by making measurements at three different nadir angles, looking both fore and aft, allowing alignment with the wavefronts of three different groups of waves.

6. CONCLUSIONS

In this paper we have attempted to show that a wide variety of atmospheric structure perturbations result in structure perturbations of the IR radiance seen from space. These atmospheric structures include both spatially extended GW fields and localized structures associated with TI layers. Radiative effects can be seen in a number of bands, including the CO_2 bands at 4.3 μm and 15 μm, and affect both BTH (near nadir and sub-limb) and ATH (limb) LOSs. Knowledge of atmospheric RT is an essential tool to infer the properties of the perturbing processes from radiance measurements by remote sensing.

7. ACKNOWLEDGEMENTS

We are grateful to Kent Miller and Paul Bellaire of the Air Force Office of Scientific Research for support of this work. It was also partially funded by the NASA Sun-Earth Connection program in Ionosphere, Thermosphere, and Mesosphere Physics. We acknowledge the enthusiastic encouragement of Robert O'Neil and the assistance of MSX team members in carrying out the analysis and modeling of the MSX data. We are grateful to Gary Swenson and the Waves Explorer team, especially Joan Alexander and John Kumer, for the opportunity to participate in the elaboration of the Waves Explorer experiment concept.

8. REFERENCES

1. Taylor, M. J., and M. A. Hapgood, Identification of a thunderstorm as a source of short period gravity waves in the upper atmospheric nightglow emissions, *Planet. Space Sci.*, **36**, 975-985, 1988.
2. Dewan, E. M., R. H. Picard, R. R. O'Neil, H. A. Gardiner, J. Gibson, J. D. Mill, E. Richards, M. Kendra, and W. Gallery, MSX satellite observations of thunderstorm-generated gravity waves in mid-wave infrared images of the upper stratosphere, *Geophys. Res. Lett.*, **25**, 939-942, 1998.
3. Dewan, E. M., and R. E. Good, Saturation and the "universal" spectrum for vertical profiles of horizontal scalar winds in the atmosphere, *J. Geophys. Res.,* **91**, 2742-2748, 1986.
4. Dewan, E. M., Saturated-cascade similitude theory of gravity wave spectra, *J. Geophys. Res.*, **102**, 29799-29817, 1997.
5. Gossard, E. E., and W. H. Hooke, *Waves in the Atmosphere,* Elsevier, New York, 1975.
6. Makhlouf, U. B., R. H. Picard, M. J. Taylor, and J. R. Winick, Gravity waves and vertical diffusion in the lower thermosphere from 557.7 nm airglow, *Adv. Space Res.*, **19**, 583, 1997.
7. Makhlouf, U. B., R. H. Picard, J. R. Winick, and T. F. Tuan, A model for the response of the atomic oxygen 557.7nm and the OH Meinel airglow to atmospheric gravity waves in a realistic atmosphere, *J. Geophys. Res.,* **103**, 6261-6269, 1998.
8. Dao, P. D., R. Farley, X. Tao, and C. S. Gardner, Lidar observations of the temperature profile between 25 and 103 km: Evidence of strong tidal perturbations, *Geophys. Res. Lett.,* **22**, 2825-2828, 1995.
9. Tao, X., and C. S. Gardner, Heat flux observations in the mesopause region above Haleakala, *Geophys. Res. Lett.,* **22**, 2829-2832, 1995.
10. Huang, T. Y., H. Hur, T. F. Tuan, X. Li, E. M. Dewan, and R. H. Picard, Sudden narrow temperature inversion-layer formation in ALOHA-93 as a critical-layer phenomenon, *J. Geophys. Res.*, **103**, 6323-6332, 1998.
11. Taylor, M. J., D. N. Turnbull, and R. P. Lowe, Spectrometric and imaging measurements of a spectacular gravity wave event observed during the ALOHA-93 campaign, *Geophys. Res. Lett.*, **22**, 2848-2852, 1995.
12. Dewan, E. M., and R.H. Picard, On mesospheric bores, *J. Geophys. Res.*, **103**, 6295-6305, 1998.
13. Dewan, E. M., and R.H. Picard, On the origin of mesospheric bores, *J. Geophys. Res.*, **106**, 2921-2927, 2001.
14. Goody, R. M., and Y. L. Yung, *Atmospheric Radiation*, Oxford University Press, New York, 1989.
15. Wintersteiner, P. P., R. H. Picard, R. D.Sharma, J. R. Winick, and R. A. Joseph, Line-by-line radiative excitation model for the non-equilibrium atmosphere: Application to CO_2 15-μm emission, *J. Geophys. Res.*, **97**, 18083-18117, 1992.
16. Nebel, H., P. P. Wintersteiner, R. H. Picard, J. R. Winick, and R. D. Sharma, CO_2 non-LTE radiative excitation and infrared dayglow at 4.3 μm: Application to SPIRE data, *J. Geophys. Res.*, **99**, 10409-10420, 1994.
17. Picard, R. H., R. R. O'Neil, H. A. Gardiner, J. Gibson, J. R. Winick, W. O. Gallery, A. T. Stair, Jr., P. P. Wintersteiner, E. R. Hegblom, and E. Richards, Remote sensing of discrete stratospheric gravity-wave structure at 4.3-μm from the MSX satellite, *Geophys. Res. Lett.*, ***25***, 2809-2812, 1998.
18. Hersé, M., Waves in the OH emissive layer, *Science,* **225**, 172-174, 1984.
19. Ross, M. N., A. B. Christensen, C.-L. Meng, and J. F. Carbary, Structure in the UV nightglow observed from low earth orbit, *Geophys. Res. Lett.,* **19**, 985-988, 1992.
20. Mende, S. B., G. R. Swenson, S. P. Geller, and K. A. Spear, Topside observation of gravity waves, *Geophys. Res. Lett.,* **21**, 2283-2286, 1994.
21. Mende, S. B., S. P. Geller, and G. R. Swenson, Gravity wave modulated airglow observation from spacecraft (abstract), *Eos Trans. AGU,* **78**(17), Spring Meet. Suppl., S237, 1997.

22. Wu, D. L., and J. W. Waters, Gravity-wave-scale temperature fluctuations seen by the UARS MLS, *Geophys. Res. Lett.,* **23**, 3289-3292, 1996a.
23. Wu, D. L., and J. W. Waters, Satellite observations of atmospheric variances: A possible indication of gravity waves, *Geophys. Res. Lett.,* **23**, 3631-3634, 1996b.
24. McLandress, C., M. J. Alexander, and D. L. Wu, Microwave Limb Sounder observations of gravity waves in the stratosphere: A climatology and interpretation, *J. Geophys. Res.*, **105**, 11947-11967, 2000.
25. Fetzer, E. J., and J.C. Gille, Gravity wave variance in LIMS temperatures, Part I. *J. Atmos. Sci.,* **51**, 2461-2483, 1994.
26. Mill, J. D., R. R. O'Neil, S. Price, G. J. Romick, O. M. Uy, E. M. Gaposchkin, G. C. Light, W. W. Moore, Jr., T. L. Murdock, and A. T. Stair, Jr., Midcourse Space Experiment, *J. Spacecraft Rockets,* **31**, 900-907, 1994.
27. O'Neil, R. R., H. A. B. Gardiner, J. Gibson, C. Humphrey, R. Hegblom, M. E. Fraser, M. Kendra, P. Wintersteiner, and C. Rice, Midcourse Space Experiment (MSX), *Proc. Soc. Photo. Opt. Instrum. Eng*., **2223**(25), 264-273, 1994.
28. Clough, S. A., F. X. Kneizys, E. P. Shettle, and G. P. Anderson, Atmospheric radiance and transmittance: FASCOD2, *Sixth Conference on Atmospheric Radiation*, pp. 141-144, American Meteorological Society, Boston, 1986.
29. Alexander, M. J., Interpretations of observed climatological patterns in stratospheric gravity wave variance, *J. Geophys. Res.*, **103**, 8627-8640, 1998.
30. Hines, C.O., Internal atmospheric gravity waves at ionospheric heights, *Can. J. Phys.,* **38**, 1441-1481, 1960.
31. Fritts, D. C., and M. Alexander, The WAVES Explorer: Quantification of gravity wave forcing of the MLTI, *Eos Trans. AGU*, **80**(17), S236, 1999.
32. Kumer, J. B., R. Rairden, A. E. Roche, V, Kotsubo, T. C. Nast, and J. R. Olson, Test for mechanical-cooler-induced noise in a low-noise infrared 2D detector array: Spaceborne application for sensing wave structure in thermal CO_2 emission, *Proc. Soc. Photo. Opt. Instrum. Eng*., **4306**, 1-12, 2001.

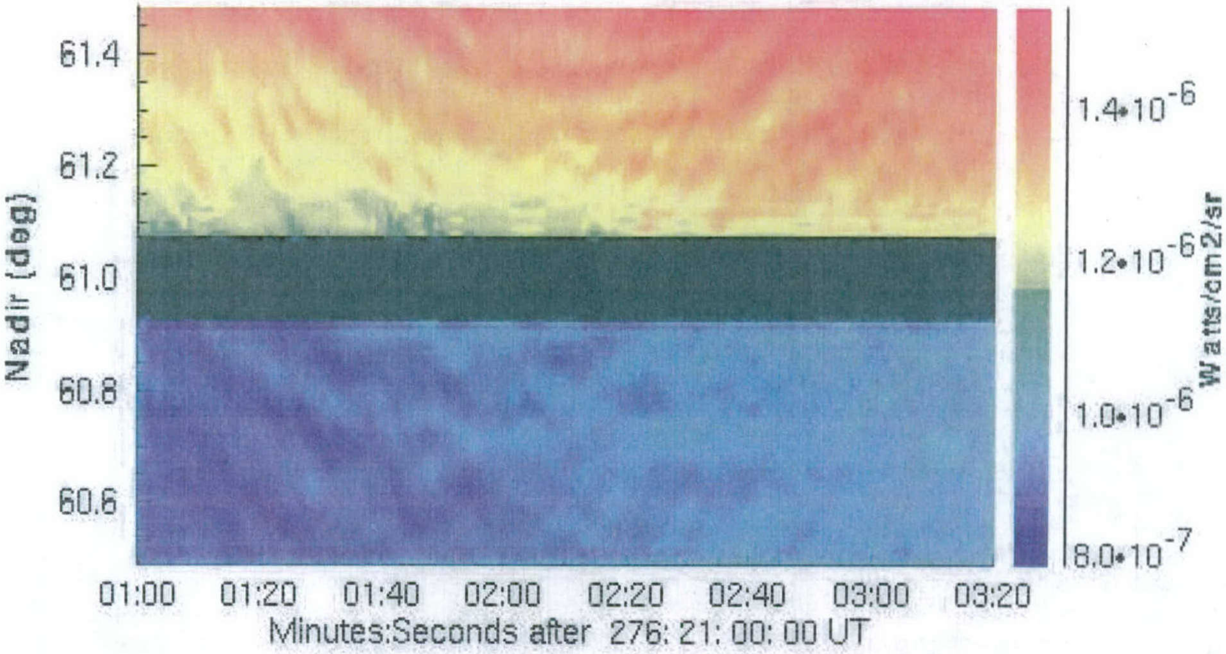

Figure 1: MSX 4.3-µm below-the-horizon (BTH) image of quasi-sinusoidal circular gravity-wave structure generated by a compact thunderstorm.[2] Radiance originates from an altitude range of about 20 km centered near 40 km altitude. Lower part of image is from the narrower B1 band and upper part from the wider B2 band; B1 is only sensitive to stratospheric structure while B2 has some sensitivity to tropospheric structure.

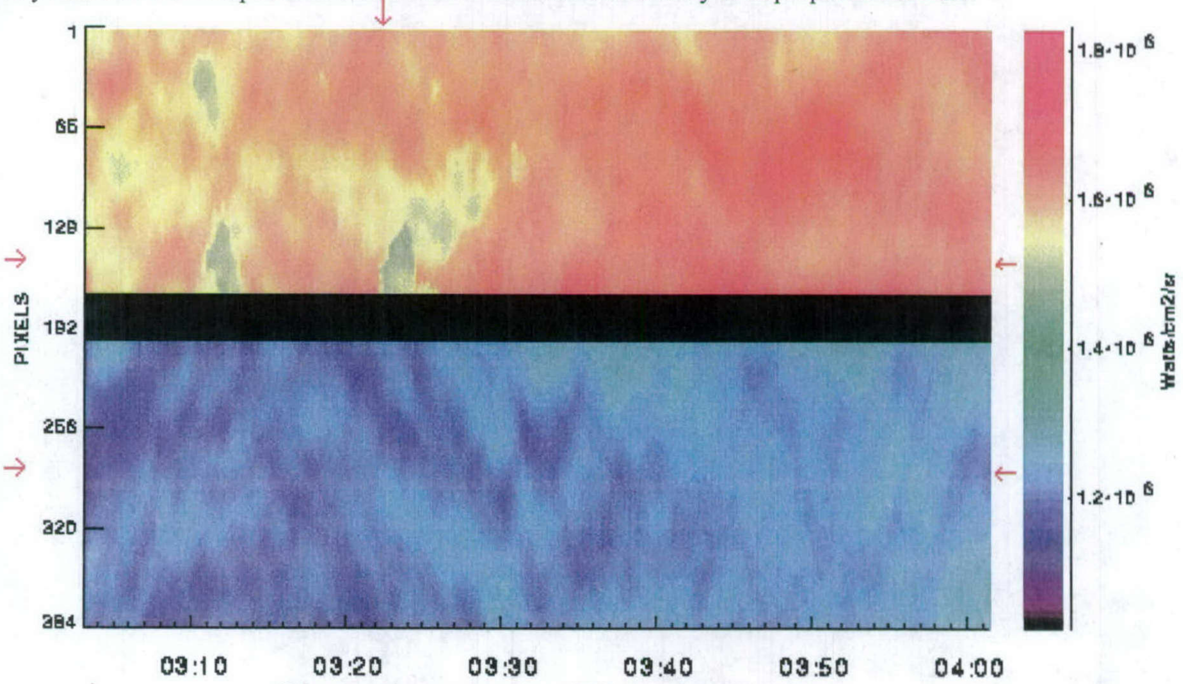

Figure 2: MSX 4.3-µm BTH image of broader-spectrum structure from superposed gravity waves originating near 40 km altitude.[17]

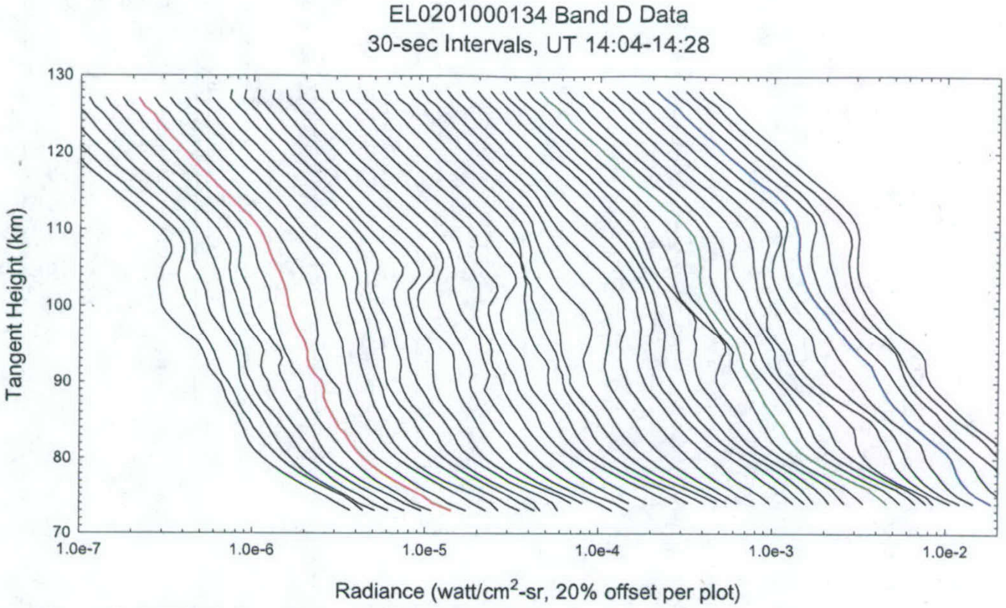

Figure 3: MSX limb-radiance profiles taken 30 s apart in a view direction orthogonal to the velocity vector, showing considerable wave structure in the 90-110 km region.

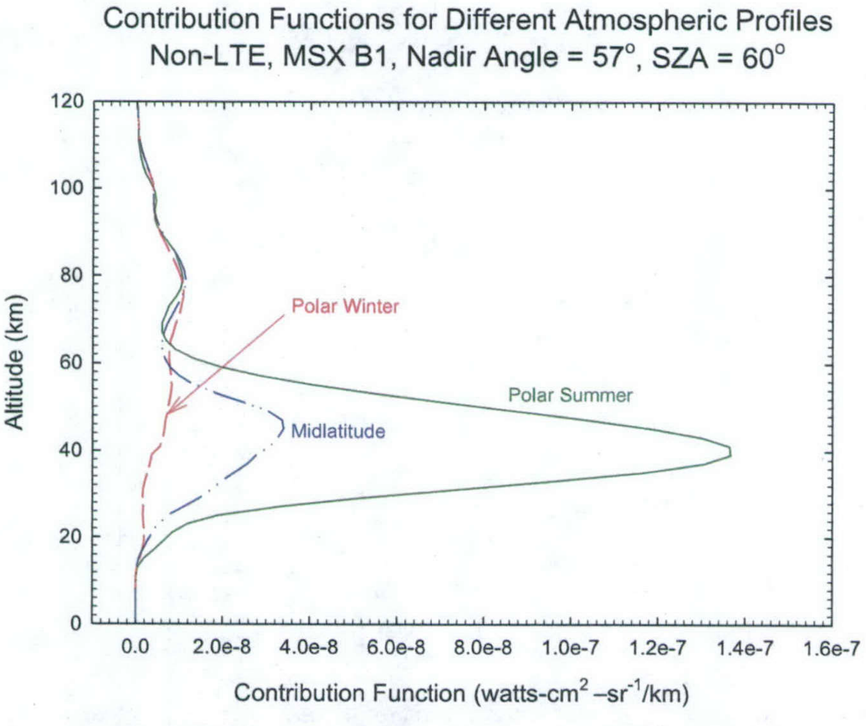

Figure 4: MSX B1-band contribution function (CF) for three different model atmospheres—polar summer (solid), midlatitude (dash – double dot), and polar winter (dashed).

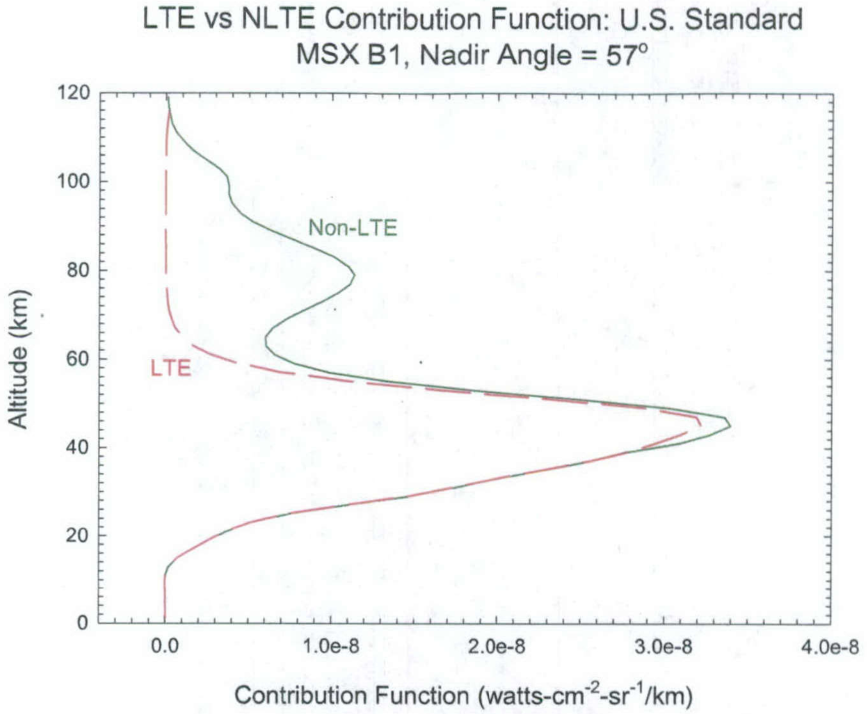

Figure 5: MSX B1-band non-LTE (solid) and LTE (dashed) CFs for a midlatitude atmosphere.

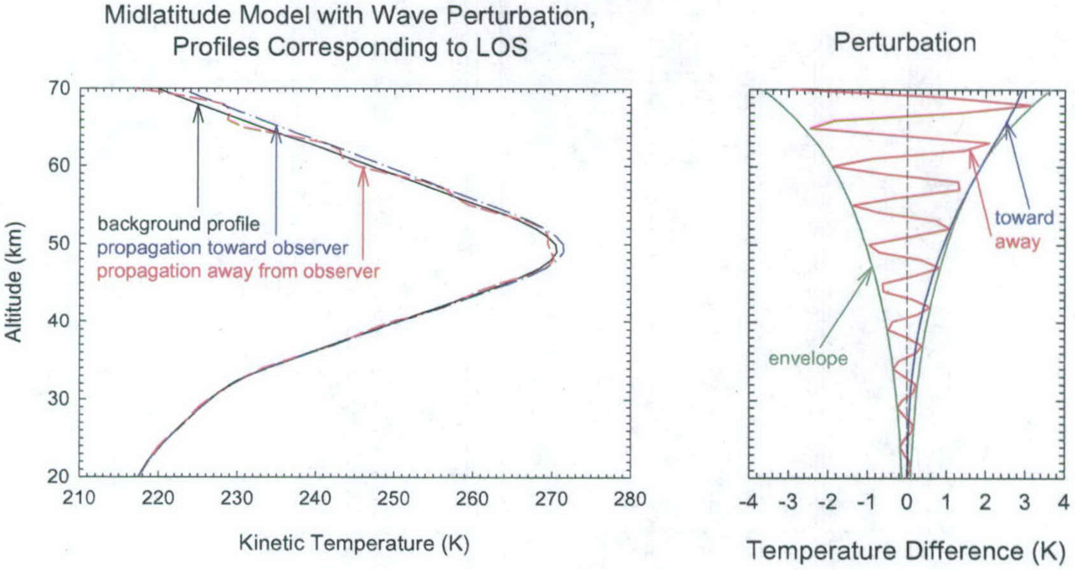

Figure 6: Unperturbed kinetic temperature (background profile) in the vicinity of stratopause, along with altitude profiles of wave-perturbed temperature at points along lines-of-sight (LOSs) that (1) coincide with a phase front (propagation toward observer) and (2) cut across phase fronts (propagation away from observer). The calculation assumes MSX orbital altitude, a nadir angle of 57°, and a wave of vertical (horizontal) wavelength 10 km (32 km). For the aligned case the wave perturbations along the LOS are all in phase, whereas in the misaligned case the contributions oscillate around the unperturbed profile, leading to cancellation of the effect of the perturbation in the column-integrated radiance. The right-hand portion of the figure plots the temperature perturbation along these two LOSs and also shows the exponential growth with height of the envelope of the perturbation amplitude.

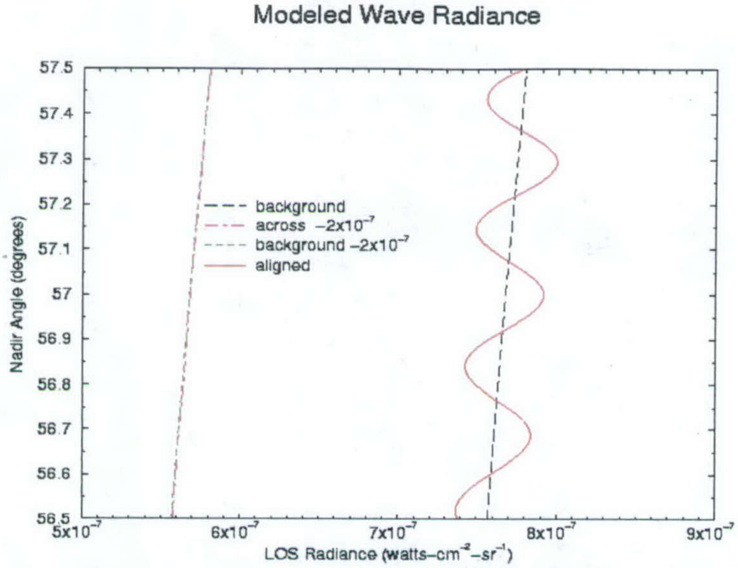

Figure 7: 4.3-μm volume emission rate perturbations corresponding to the temperature perturbations shown in Figure 6 plotted versus nadir angle. The right-hand curves shows the background and perturbed radiance as a function of nadir angle over the 1° MSX field-of-view, centered on the angle (57°) where the LOS is aligned along a wavefront. The left-hand curves show the same quantities when the direction of wave propagation is reversed so that the LOS now cuts across wavefronts and have been displaced by subtracting 2×10^{-7} for clarity.

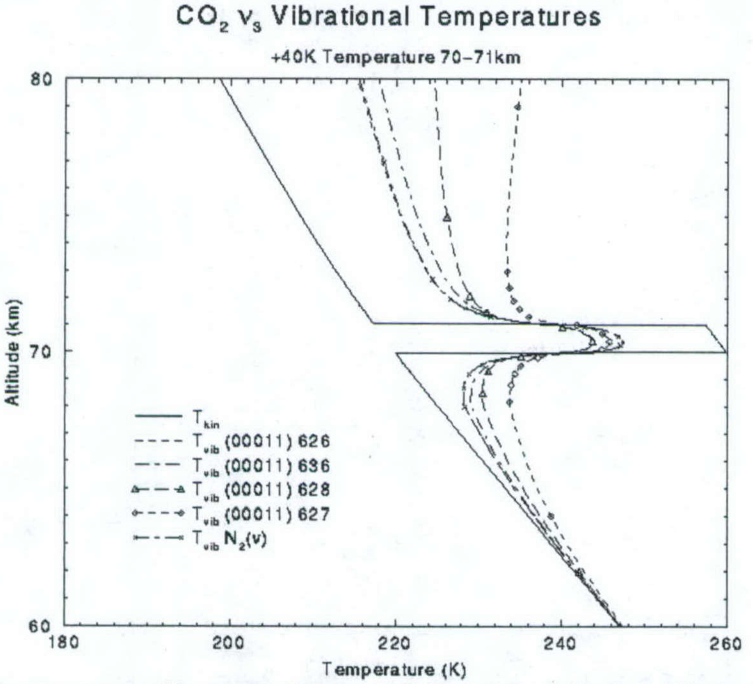

Figure 8: Temperature profile perturbed by a +40 K layer 1-km wide at an altitude of 70 km. Vibrational temperature responses are shown for a number of radiating CO_2 4.3-μm states and for N_2 vibration, which is strongly coupled to the CO_2 ν_3 states by collisions. Notice that radiative transport not only reduces the magnitude of the perturbation within the perturbed temperature layer but also extends the perturbation far outside the region of the temperature perturbation, especially on the high-altitude side of the layer.

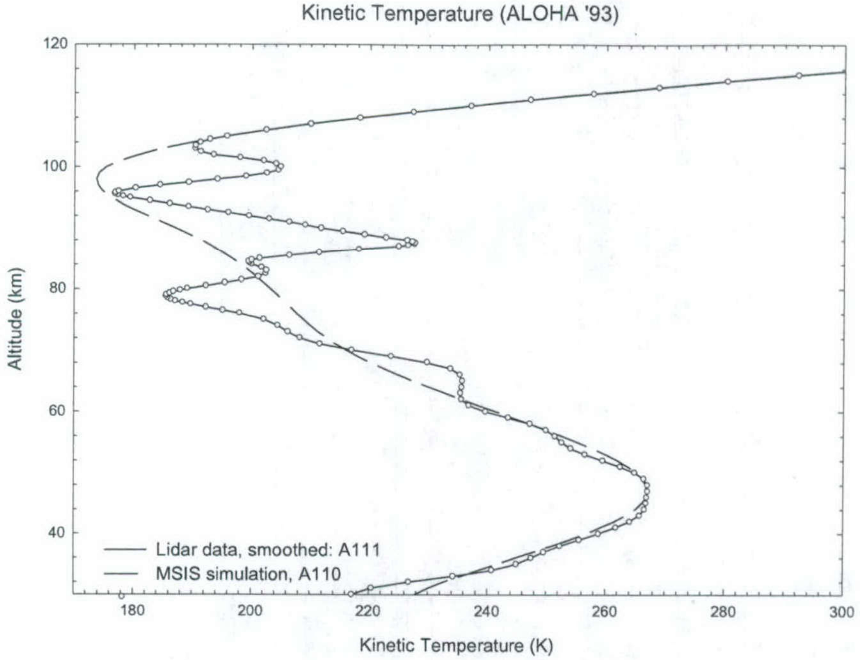

Figure 9: Lidar temperature profile measured during the ALOHA-93 Campaign from the AF Maui Optical Station,[8] showing several prominent temperature-inversion (TI) layers. A corresponding smooth climatological profile is also shown.

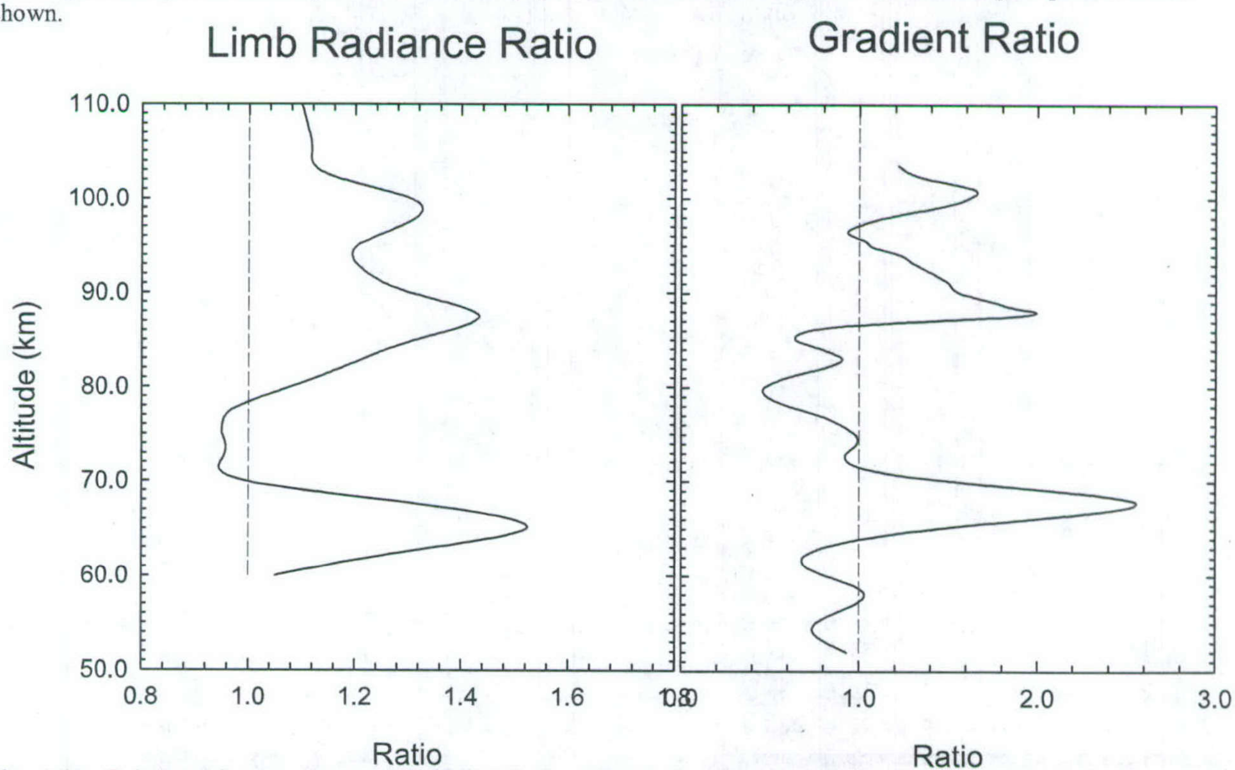

Figure 10: Relative 4.3-μm radiance perturbation (left) and vertical-radiance-gradient perturbation (right) for the perturbed atmosphere corresponding to the ALOHA-93 lidar profile of Figure 9 and the corresponding smooth profile.

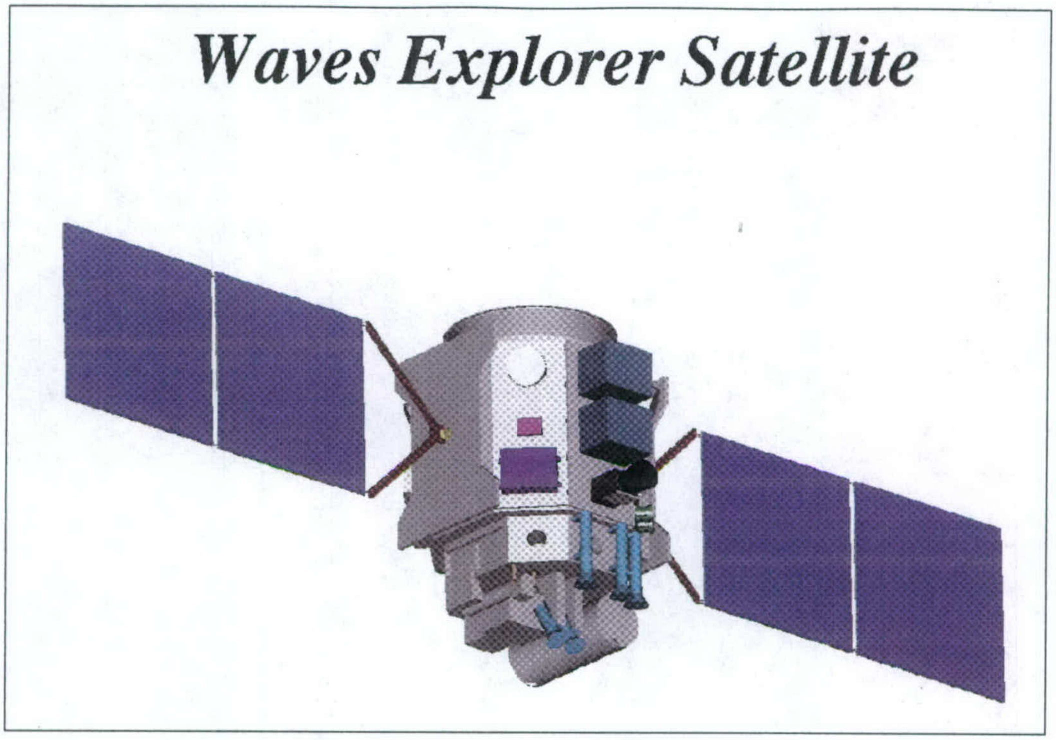

Figure 11: Artist's conception of Waves Explorer satellite.